Journal of Luminescence 202 (2018) 523–531

Contents lists available at ScienceDirect

Journal of Luminescence

journal homepage: www.elsevier.com/locate/jlumin

Temperature dependent Cr^{3+} photoluminescence in garnets of the type $X_3Sc_2Ga_3O_{12}$ (X = Lu, Y, Gd, La)

Beata Malysa[a,b,*], Andries Meijerink[b,**], Thomas Jüstel[a]

[a] Münster University of Applied Sciences, Stegerwaldstrasse 39, D-48565 Steinfurt, Germany
[b] University Utrecht, Princetonplein 1, NL-3584 Utrecht, The Netherlands

ARTICLE INFO

Keywords:
Cr^{3+} photoluminescence
Garnets
Near infrared emitting phosphors
Racah parameters
Thermal quenching
Phosphor converted LEDs
On-chip phosphor
3*d*-3*d* emission

ABSTRACT

Broad band near-infrared (NIR) light sources have great potential, e.g., in optical communication and non-invasive medical imaging. Here we report the optical properties of $X_3Sc_2Ga_3O_{12}$ (X = Lu, Y, Gd, La) garnets doped with Cr^{3+} showing efficient $^4T_2 \rightarrow {}^4A_2$ broad band NIR emission between 600 and 1000 nm. The chromium-doped garnets were investigated in view of their capability for blue to NIR conversion in high power phosphor converted LEDs (pcLEDs). Typical high power (In,Ga)N LEDs reach junction temperatures up to 450 K. Hence, the photoluminescence (PL) quenching temperature is a crucial parameter for on-chip phosphors. The Cr^{3+}-doped garnets reveal very high quenching temperatures for the broad band NIR emission, ~700 K for $Lu_3Sc_2Ga_3O_{12}$, $Y_3Sc_2Ga_3O_{12}$, $Gd_3Sc_2Ga_3O_{12}$, and 450 K for $La_3Sc_2Ga_3O_{12}$. The high quenching temperatures are in line with a small Stokes shift (~2400 cm^{-1}) and weak electron-phonon coupling. To gain further insight in the luminescence properties, low temperature photoluminescence measurements were done. The optical properties of Cr^{3+} ions in garnets were analyzed in terms of the crystal field strength, Racah parameters, and phonon coupling parameters. The suitability for application in pcLEDs for high power broad band NIR sources was confirmed by emission measurements of ceramic pellets upon blue LED excitation.

1. Introduction

The invention of efficient blue (In,Ga)N light emitting diodes (LEDs) caused the rapid development of LED based solid state lighting (SSL). Nowadays, white phosphor converted (pc) LEDs composed of a blue (In,Ga)N chip and a yellow $Y_3Al_5O_{12}:Ce^{3+}$ (YAG:Ce) phosphor are a part of our daily life, since they provide many advantages over old-fashioned incandescent lamps and compact fluorescent tubes [1,2]. In the past decades many phosphors and blends have been invented and optimized to generate white LED lamps covering the full technically required color temperature range [3]. The development of high power pcLEDs with high reliability and wall-plug efficiency requires radiation converters, which exhibit strong absorption in the energy range where the pump source emits radiation, high quantum yield, very good chemical and thermal stability, and absence of emission saturation at high fluxes [4]. Moreover, on-chip phosphors should not suffer from thermal quenching up to 450 K, a typical LED junction temperature that may be even exceeded by internal self-heating by the Stokes loss [5]. It is well known, that the photoluminescence efficiency of some phosphors strongly depends on ambient temperature and usually decreases at elevated temperature due to a higher probability of nonradiative transitions [6,7]. Thus, the luminescent converters used for pcLEDs are required to have high thermal quenching temperature ($T_{1/2}$ > 200 °C), i.e. a small emission loss during a high power LED operation.

The realization of high performance phosphor for pcLEDs or laser diodes is a huge challenge because it is very difficult to find materials that fulfill all of the aforementioned criteria. The thermal quenching temperature of photoluminescence is a crucial parameter for LED phosphors and depends strongly on the structural rigidity of the host lattice. The decline of PL efficiency with increasing temperature can be minimized in host lattices like garnets, nitrides, or oxy-nitrides [8]. The best known commercially available LED phosphors with a quenching temperature $T_{1/2}$ higher than 500 K are $Y_3Al_5O_{12}:Ce^{3+}$ [9], (Ca,Sr)AlSiN$_3$:Eu^{2+} [10], $SrSi_2O_2N_2:Eu^{2+}$ [11], and Ca-α-SiAlON:Eu^{2+} [12].

The availability of efficient and high power blue (In,Ga)N LEDs is promising for the manufacturing of high power NIR LEDs by pumping of a suitable NIR phosphor by a blue or NUV emitting (In,Ga)N LED [13]. Such near infrared emitting pcLEDs are a potential alternative for commonly used NIR sources such as incandescent bulbs, halogen lamps, or silicon carbide heating elements (very broad Planck-like emission

* Corresponding author at: Münster University of Applied Sciences, Stegerwaldstrasse 39, D-48565 Steinfurt, Germany.
** Corresponding author.
E-mail addresses: beata.malysa@fh-muenster.de (B. Malysa), a.meijerink@uu.nl (A. Meijerink), tj@fh-muenster.de (T. Jüstel).

https://doi.org/10.1016/j.jlumin.2018.05.076
Received 15 February 2018; Received in revised form 3 May 2018; Accepted 30 May 2018
Available online 31 May 2018
0022-2313/

spectrum) and near-infrared GaAs or (Al,Ga)As LEDs (narrow band EL spectra). The mentioned broad band NIR sources have a notoriously low energy efficiency, whereas the application of NIR LEDs in spectroscopy, optical communication, phototherapy, and non-invasive medical imaging (e.g., optical coherence tomography, monitoring of blood oxygenation) is sometimes hampered by their too narrow emission band and the spectral shift with drive conditions, i.e. junction temperature and power density [14–19]. Therefore, there is a clear need for efficient broad band NIR light sources and NIR pc-LEDs have great potential.

Since the spectral conversion from blue/NUV to NIR involves significant energy dissipation, the main challenge is in the optimization of novel NIR emitting materials for solid state light sources is to realize a high $T_{1/2}$ which can be done by minimizing the Stokes shift [20]. In this work, we report the optical properties of Cr^{3+}-doped $Lu_3Sc_2Ga_3O_{12}$ (LuSGG), $Y_3Sc_2Ga_3O_{12}$ (YSGG), $Gd_3Sc_2Ga_3O_{12}$ (GSGG), and $La_3Sc_2Ga_3O_{12}$ (LaSGG) in view of their potential application as blue to NIR converters in pcLEDs. Garnets are (photo)-chemically and thermally stable hosts, which exhibit a high structural rigidity and a rather high thermal conductivity compared to other ceramics. Scandium containing garnets were developed as a type of tunable Cr^{3+}-doped crystals and as scintillators. Thus, the Cr^{3+} PL in YSGG, GSGG, and LuSGG is already well known [21], whereas we report on the optical properties of LaSGG:Cr^{3+} phosphor for the first time. However, to the best of our knowledge, there are no reports on the temperature dependence of the Cr^{3+} emission in these materials, which is a crucial parameter for the on-chip phosphors. Here, we report and discuss the broad band emission spectra of Cr^{3+} in $X_3Sc_2Ga_3O_{12}$ (X = Lu, Y, Gd, La) and the influence of the lattice parameters on the luminescence properties with regard to the crystal field strength and Racah parameters. Additionally, thermal quenching measurements were performed in order to examine the thermal stability of the broad band Cr^{3+} emission. The measurements at cryogenic temperatures provide insight into spectral details which are not observed at room temperature (RT). The suitability of the synthesized phosphors for NIR emitting pcLEDs are confirmed by positive results from measurements of ceramic pellets using high power blue LEDs as a pump source.

2. Experimental section

2.1. Synthesis

The microcrystalline powders of XSGG (X = Lu, Y, Gd, La) doped with 1% Cr^{3+} were synthesized by solid state reaction in air. As starting materials Y_2O_3 (Treibacher Industrie AG, 99.99%), La_2O_3 (Treibacher Industrie AG, 99.995%), Gd_2O_3 (Treibacher Industrie AG, 99.99%), Lu_2O_3 (Treibacher Industrie AG, 99.99%), Sc_2O_3 (Treibacher Industrie AG, 99.99%), Ga_2O_3 (Alfa Aesar, 99.995%), and Cr_2O_3 (Alfa Aesar, 99.95%) were used. The stoichiometric amounts of raw materials were ground in an agate mortar with acetone as a grinding media. The powder blends were transferred into corundum crucibles and calcined three times at 1400 °C for 6 h with intermediate grinding steps. The two intermediate grinding steps were necessary to obtain powders of single phase and to improve their homogeneity.

The μm-scale powders thus obtained were isostatically pressed by a Specac hydraulic press in a 13 mm diameter pellet die. To obtain ca. 1.0 mm thick discs, approximately 300 mg of powders were compacted for 5 min using 6 t-force. The pellets were fired at 1000 °C for 6 h in air to remove organic compounds, which have been used as a binder as well as to increase the density of sintered pellets.

2.2. Characterization

To test phase purity of the materials synthesized, X-ray diffraction patterns were measured on a Rigaku MiniFlex II diffractometer. As a radiation source a copper X-ray tube with Cu Kα radiation (λ = 1.54 Å) was used. The samples were examined in the region of 2θ between 10° and 80° with a scanning rate 10° per min.

Excitation and emission spectra were recorded on an Edinburgh Instruments FSL 920 spectrometer equipped with a 450 W Xe arc lamp, mirror optics for powder samples and a cooled (− 20 °C) single-photon counting photomultiplier from Hamamatsu (R2658P), which is sensitive up to 1010 nm. The correction file for the emission spectra was obtained from calibration with a tungsten incandescent lamp certified by NPL (National Physics Laboratory, UK). Diffuse reflection spectra were recorded on an Edinburgh Instruments FS900 spectrometer equipped with a 450 W Xe arc lamp and a cooled single-photon counting photomultiplier (Hamamatsu R928). $BaSO_4$ (Sigma-Aldrich, 99.99%) was used as a reflectance standard. For recording excitation and emission spectra at 3 K a He-cryostat "Optistat AC-V 12" from Oxford Instruments was introduced in the above described spectrometer. Thermal quenching (TQ) curves were recorded in a cryostat "MicrostatN" from Oxford Instruments. Measurements were carried out from 77 to 500 K in 50 K steps. For TQ measurements in the range from 350 to 800 K an in-house constructed sample holder was used. This holder comprises a heater located underneath the cavity for the sample and is made of corundum ceramic. The heater comprises an ISA® -CHROM60 filament with a diameter of 0.5 mm. The housing of the sample holder was actively cooled by flowing water. The decay curves were measured using an Edinburgh Instruments FLS920 fluorescence spectrometer with a photomultiplier R2658P from Hamamatsu. The samples were excited with a Xe-μs-flash lamp.

Emission spectra of powder pellets (ø = 13 mm) were measured using 3 W high power blue InGaN LEDs with maximum emission at 451 nm or 471 nm obtained from Lumileds. The powder pellets located on the top of the LED-housing were introduced into a special Spectralon Ulbricht sphere attached to the Edinburgh Instruments FSL 920 spectrometer. The reflected light and emission were directly collected in the detector.

3. Results and discussion

3.1. Description of the crystal structure of the garnets $X_3Sc_2Ga_3O_{12}$

Garnet crystals belong to the cubic space group *Ia*-3*d* and have the chemical formula $C_3A_2D_3O_{12}$ where *C*, *A*, and *D* stand for dodecahedrally, octahedrally, and tetrahedrally coordinated lattice sites, respectively. In $X_3Sc_2Ga_3O_{12}$, Ga^{3+} ions occupy the *D* sites, Sc^{3+} ions are incorporated at the *A* sites and Lu^{3+}, Y^{3+}, Gd^{3+}, La^{3+} ions are at the *C* sites [22].

Trivalent chromium has an [Ar]$3d^3$ electron configuration and due to high crystal field stabilization energy of the d^3 configuration, Cr^{3+} ions prefer octahedral coordination. Therefore, we predict a chromium substitution mainly on the Sc^{3+} sites. Additionally, the similarity of ionic radii of Sc^{3+} (0.885 Å) and Cr^{3+} (0.755 Å) ions as well as their identical charge and similar electronegativity all favor Cr^{3+} substitution on the octahedral Sc^{3+} site. The crystal ionic radius of Ga^{3+} in 4-fold coordination is 0.610 Å and the crystal ionic radii of Lu^{3+}, Y^{3+}, Gd^{3+}, and La^{3+} ions in 8-fold coordination are 1.12 Å, 1.16 Å, 1.19 Å and 1.30 Å, respectively (Table 1) [23]. Hence, it is unlikely that trivalent chromium ions replace these ions at the tetrahedral *D* sites and

Table 1
Ionic radii of X = Lu, Y, Gd, La ions in dodecahedral coordination, Sc^{3+} – O^{2-} and X^{3+} – O^{2-} distances, lattice parameters a = b = c, and density of the $X_3Sc_2Ga_3O_{12}$ garnets [25].

	X^{3+} ionic radius [Å]	Sc – O distance [Å]	X – O distance [Å]	a = b = c [Å]	Density [g/cm^3]
LuSGG	1.12	1.993	2.490	12.26	7.53
YSGG	1.16	2.018	2.522	12.42	5.25
GSGG	1.19	2.041	2.550	12.56	6.46
LaSGG	1.30	2.086	2.607	12.84	5.70

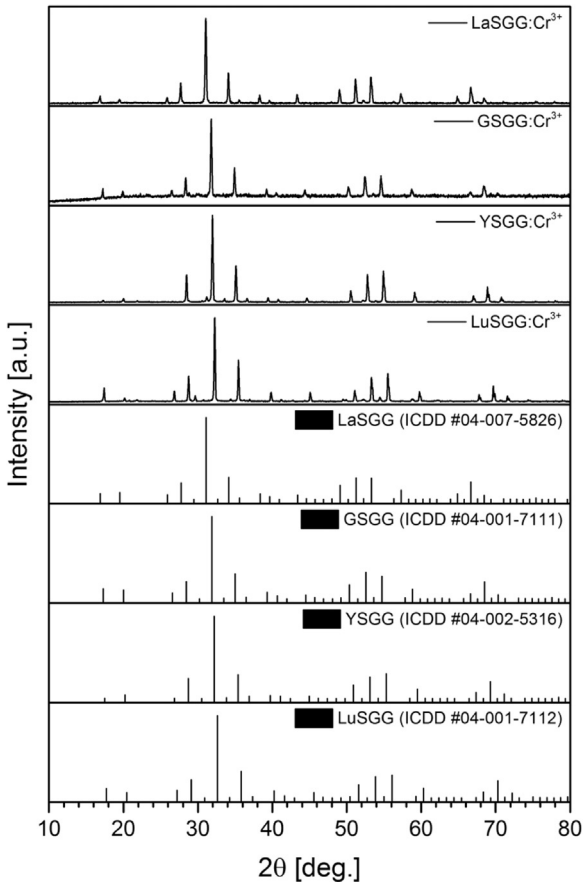

Fig. 1. XRD patterns of microcrystalline powders of XSGG:1%Cr^{3+} (X = Lu, Y, Gd, La) and ICDD reference data [25].

dodecahedral *C* sites due to the much larger difference in ionic radii and the difference in coordination number. Variation of the crystal composition of the garnets results in systematic changes in the crystal field strength acting on Cr^{3+} ions. The lattice parameters in XSGG crystals progressively increase with increasing ionic radii of the ions incorporated at the C sites ($X = Lu^{3+} < Y^{3+} < Gd^{3+} < La^{3+}$). This change reflects the increasing distances between Sc^{3+} and X^{3+} and their neighboring oxygen ions (Table 1). As the crystal field (CF) splitting increases with decreasing distance between cation and ligands (R) ($10Dq \sim (1/R^5)$) [24], we predict the smallest CF splitting for Cr^{3+} substitution on Sc^{3+} sites in LaSGG in view of the largest Sc – O distance in this structure.

3.2. Phase formation – XRD patterns

Crystal structure and phase purity of the XSGG:Cr^{3+}(1%) (X = Lu, Y, Gd, La) phosphors were explored by taking X-ray diffraction patterns that are plotted in Fig. 1. The position and relative intensities of the observed peaks match very well the reference data and there is no evidence for the presence of impurity phases in the samples.

The position of peaks in the diffraction patterns changes depending on the size of the ion at the C crystallographic sites. The XRD peaks in LaSGG sample are slightly shifted to the lower diffractions angles if compared with the peaks in LuSGG sample. This is consistent with an expansion of the host lattice and increase in the lattice parameters due to the larger ionic radius of La^{3+} in comparison to Lu^{3+}.

In the XRD graph of the $Gd_3Sc_2Ga_3O_{12}$:Cr^{3+}(1%) (Fig. 1), a higher background noise is observed and has been already reported in Cr^{3+} doped $GdAl_3(BO_3)_4$ [26] and $GdMgB_5O_{10}$ [27]. The origin of the background in powder diffraction can be related to a strong interaction

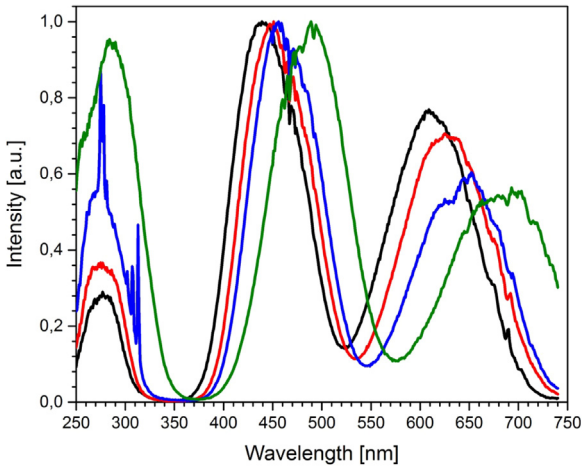

Fig. 2. Excitation spectra of LuSGG:1%Cr^{3+} (black line), YSGG:1%Cr^{3+} (red line), GSGG:1%Cr^{3+} (blue line), and LaSGG:1%Cr^{3+} (green line) recorded for 760 nm emission at room temperature.

of gadolinium atoms with Cu Kα radiation. The absorption edge of Cu Kα radiation is 8.05 keV and is similar to the energy of the L_3 absorption edge of Gd (E_{L3} = 7.24 keV) [28]. Thus, the incident radiation has sufficient energy to promote L electrons from their ground states. Subsequent recombination of electrons can produce X-ray emission that is scattered in all directions and results in an increase of the XRD background [29].

3.3. Optical properties at room temperature

Excitation spectra of LuSGG, YSGG, GSGG, and LaSGG doped with 1% Cr^{3+} were measured for a single emission wavelength (λ_{em} = 760 nm) at room temperature and are shown in Fig. 2. There are three excitation bands located in the UV, blue/cyan and deep red spectral range (Table 2). The excitation bands are attributed to the $^4A_2 \rightarrow {}^4T_1$ (^4P), $^4A_2 \rightarrow {}^4T_1$ (^4F) and $^4A_2 \rightarrow {}^4T_2$ (^4F) transitions of Cr^{3+}, respectively. In the UV region, the excitation band of LaSGG:Cr displays a shoulder at around 260 nm (38,462 cm^{-1}). It can correspond to an overlap of the O^{2-} - Cr^{3+} charge transfer band (CT) with the $^4A_2 \rightarrow {}^4T_1$ (^4P) d-d transition band.

The sharp lines superimposed on the $^4A_2 \rightarrow {}^4T_1$ (^4P) excitation band in GSGG are due to 4f–4f transitions of Gd^{3+}. The most intense peaks around 275 nm and 313 nm are assigned to the $^8S_{7/2} \rightarrow {}^6I_J$ and $^8S_{7/2} \rightarrow {}^6P_J$ electronic transitions, respectively [30]. The observation of the excitation lines of Gd^{3+} confirms that Gd^{3+} sensitizes the Cr^{3+} emission. Moreover, some weak and narrow peaks at 689 nm (for LuSGG), 692 nm (for YSGG), and 694.5 nm (for GSGG) are observed. These lines are assigned to the spin-forbidden transition from the $^4A_2$ ground state to the ^2E (^2G) excited state.

Fig. 3 displays normalized photoluminescence spectra of Cr^{3+} in LuSGG, YSGG, GSGG, and LaSGG garnets recorded at room temperature for the excitation at 440 nm, 450 nm, 460 nm, and 480 nm, respectively. All samples emit in the NIR range. The emission spectra extend from 600 to 1000 nm (or even longer wavelengths for LaSGG:Cr) and consist mostly of broad bands corresponding to the spin-allowed $^4T_2 \rightarrow {}^4A_2$ transition. The values of a full width at half maximum (FWHM) vary among the investigated Cr-doped garnets (Table 2). The FWHM for LaSGG:Cr is around 145 nm (2160 cm^{-1}), while the FWHM for the LuSGG:Cr is two times smaller, viz. 73 nm (1406 cm^{-1}). The narrow bandwidth for the Cr^{3+} emission in LuSGG is partly caused by the presence of relatively strong $^2E \rightarrow {}^4A_2$ line (also known as R-line) emission superimposed on the $^4T_2 \rightarrow {}^4A_2$ emission band. The spin-forbidden $^2E \rightarrow {}^4A_2$ transition of Cr^{3+} at room temperature is only visible in LuSGG and YSGG. The sharp lines are on the shorter wavelength edge

Table 2
Maximum of the peaks of the Cr^{3+} electronic transitions in the XSGG:1%Cr^{3+} (X = Lu, Y, Gd, La) garnets and FWHM (full width at half maximum) for the $^4T_2$ emission at room temperature.

	λ_{ex} ($^4A_2 \rightarrow {}^4T_1(^4P)$)	λ_{ex} ($^4A_2 \rightarrow {}^4T_1(^4F)$)	λ_{ex} ($^4A_2 \rightarrow {}^4T_2(^4F)$)	λ_{em} ($^4T_2 \rightarrow {}^4A_2$)	λ_{em} ($^2E \rightarrow {}^4A_2$)	FWHM ($^4T_2 \rightarrow {}^4A_2$)
LuSGG	278 nm	446 nm	614 nm	722 nm	689 nm	73 nm (1406 cm^{-1})
YSGG	278 nm	452 nm	631 nm	740 nm	692 nm	90 nm (1611 cm^{-1})
GSGG	278 nm	460 nm	651 nm	754 nm	–	90 nm (1577 cm^{-1})
LaSGG	286 nm	490 nm	685 nm	818 nm	–	145 nm (2160 cm^{-1})

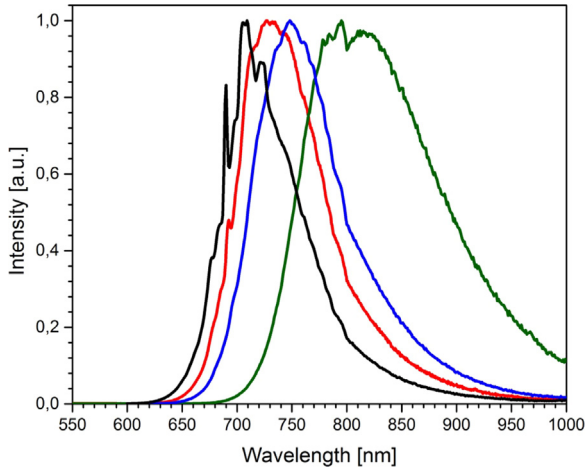

Fig. 3. Emission spectra of XSGG:1%Cr^{3+} recorded at room temperature upon excitation at 440 nm (LuSGG, black line), 450 nm (YSGG, red line), 460 nm (GSGG, blue line) and 480 nm (LaSGG, green line).

of the broad band and peak at around 689 nm and 692 nm, respectively. A characteristic dip at around 800 nm in the emission spectrum of LaSGG:Cr was identified to originate from the correction file in the NIR spectral range.

As the Cr^{3+} ion has a [Ar]$3d^3$ electron configuration, the three valence electrons are not shielded by outer shells and this gives rise to a strong interaction with the crystal field and lattice vibrations due to the spatial extension of the d electron wavefunctions in the crystals. The strong crystal field interaction for Cr^{3+} ions gives the possibility to tune photoluminescence properties of Cr-phosphors. The influence of the host lattice on the Cr^{3+} spectra is expressed by spectroscopic parameters such as the crystal field splitting (10*Dq*), and the *B* and *C* Racah parameters. In order to compare the influence of the variation in the local coordination in the different garnets structures on the Cr^{3+} luminescence, we calculated these parameters for XSGG:Cr^{3+} from the energy maxima of the $^4A_2 \rightarrow {}^4T_2$ (^4F) and $^4A_2 \rightarrow {}^4T_1$ (^4F) absorption bands. The calculated parameters for XSGG:Cr and the parameters for other Cr^{3+}-doped garnets gathered from literature are collected in Table 3.

Table 3
Crystal field splitting parameter 10*Dq*, *B* and *C* Racah parameters, and β-covalency of Cr^{3+}-doped garnets as determined from the energy values at the maxima of the $^4A_2 \rightarrow {}^4T_2(^4F)$ and $^4A_2 \rightarrow {}^4T_1(^4F)$ absorption bands (see Table 2). Spectroscopic parameters for LuAG:Cr were obtained from our work (not included here). B_0 is the free Cr^{3+} ion value and equals 918 cm^{-1}.

	Dq [cm^{-1}]	*B* [cm^{-1}]	*C* [cm^{-1}]	*Dq/B*	$\beta = B/B_0$
LuAG	1683	612	3202	2.75	0.667
YAG [33]	1640	630	3260	2.60	0.686
YGG [21]	1630	639	3250	2.55	0.696
LuSGG	1626	632	3274	2.57	0.688
YSGG	1587	635	3258	2.50	0.692
GSGG	1563	639	3221	2.45	0.696
LaSGG	1458	642	–	2.27	0.700

The population of the $^4T_2$ level at RT results in a broad band emission and is a dominant feature in XSGG:Cr^{3+} garnets. It indicates on relatively weak crystal field acting on Cr^{3+} ions in these host matrices. The crystal field strength changes in garnets depending on the metal ions residing on the C, A, and D sites (Table 3). The substitution of Ga^{3+} or/and Sc^{3+} ions for Al^{3+} on the A octahedral sites in garnets considerably decreases the crystal field strength. The presence of weaker crystal field sites in XSGG garnets results from their larger lattice constants relative to LuAG or YAG as the Sc^{3+} and Ga^{3+} ions are larger than Al^{3+} [31]. The *Dq* values for YAG:Cr and YSGG:Cr are 1640 cm^{-1} and 1587 cm^{-1}, respectively. The much higher crystal field strength in the YAG:Cr sample is reflected by a higher intensity of the R-line at 688 nm compared to YSGG sample, where the ^2E emission at 692 nm is very weak [32]. The lower value of *Dq* for Cr^{3+} ions in YSGG than in YAG is due to a larger distance between Sc^{3+} ions and their neighboring oxygen ligands (2.018 Å) in comparison to the Al^{3+} - O^{2-} distance (1.719 Å). The smaller distance for Cr^{3+} substituting on the Al^{3+} sites causes a stronger CF splitting in YAG:Cr. An interesting property is also the variation of B Racah parameters for Cr^{3+} doped XSGG garnets (Table 3). The *B* Racah parameter corresponds to the interelectron repulsion within the 3d orbitals and its values for Cr^{3+} in crystals are lower than the free – ion value, B_0 = 918 cm^{-1} [34]. The parameter *B* becomes much smaller in materials, which are characterized by a high covalent interaction between the metal ions and surrounding ligands. The higher the covalent character of the bonds, the greater delocalization of the 3d electrons of the Cr^{3+} ion occurs, resulting in decreasing electrostatic interaction and smaller *B* values. The *Dq* and Racah parameters show different sensitivity to the metal - ligand distance. The crystal field strength parameter *Dq* strongly depends on the cation - ligand distance *R* ($10Dq \sim (1/R^5)$), whereas Racah parameters reveal a stronger dependence on the host covalency which varies in a more complex manner on interionic distances and the chemical nature of the ions [35]. The increasing ionic radii of $Lu^{3+} < Y^{3+} < Gd^{3+} < La^{3+}$ ions causes an increase of the lattice constants of XSGG:Cr^{3+} garnets and an increase of the Cr^{3+}-ligand distance. It results in a clear decrease of the crystal field splitting parameter *Dq* from 1626 cm^{-1} in LuSGG to 1458 cm^{-1} in LaSGG. The influence of the host lattice on the *B* Racah parameters is not as clear and the variation for *B* obtained from the analysis of the spectral positions of the absorption bands is small (632 – 642 cm^{-1}). The small increase in *B* from Lu to La indicates an increase of the ionic character. Among four investigated Cr^{3+} doped garnets, the higher degree of covalency is reflected by the smallest β value (β = 0.688) and is observed in the LuSGG host lattice.

Decreasing crystal field strength at the octahedral sites in XSGG:Cr can be also directly observed in the excitation and emission spectra. In Fig. 2, a red shift (from X = Lu to La) of two excitation bands with maxima in the blue/cyan and deep red spectral range is observed. The red shift is attributed to an increase of the distance between Cr^{3+} and O^{2-} ions. The smaller CF splitting reduces the energy gap between the higher energy $^4T_1$ and $^4T_2$ levels and the ground state $^4A_2$ level. Likewise, the smaller energy separation between $^4T_2$ excited state and the ground state causes a red shift of the broad band emission (Fig. 3). The emission maximum at RT in LaSGG:Cr (λ_{max} = 818 nm) is red shifted by about 100 nm compared to the emission maximum in LuSGG:Cr (λ_{max} = 722 nm).

Table 4
The maxima of the excitation and emission bands of Cr^{3+} ions in XSGG (X = Lu, Y, Gd, La) at 3 K.

	λ_{ex} ($^4A_2 \rightarrow {}^4T_1$ (^4F))	λ_{ex} ($^4A_2 \rightarrow {}^4T_2$ (^4F))	λ_{em} ($^4T_2$ (^4F) $\rightarrow {}^4A_2$)	λ_{em} (^2E (^2G) $\rightarrow {}^4A_2$)
LuSGG	440 nm	607 nm	720 nm	688 nm
YSGG	450 nm	618 nm	728 nm	690 nm
GSGG	458 nm	636 nm	748 nm	694.5 nm
LaSGG	485 nm	675 nm	805 nm	–

3.4. Temperature dependence of optical properties

Since the thermal broadening has a significant impact on the luminescence properties of Cr^{3+} at room temperature, low temperature measurements were done. Measurements at liquid helium temperature reveal spectral details that are not visible at a higher temperature and allow an accurate determination of the Stokes shift and Huang-Rhys parameters, whereas temperature dependent emission spectra and decay time measurements provide insight in thermal quenching of the Cr^{3+} emission. The overview on the positions of the excitation and emission bands at 3 K is given in Table 4.

Fig. 4 displays the emission spectra of Cr^{3+} doped LuSGG, YSGG, and LaSGG recorded at 3 K upon excitation at 440 nm, 460 nm, and 480 nm, respectively. The emission spectrum of LuSGG:Cr consists of a narrow R-line positioned at 688 nm and its phonon-side bands. The emission spectrum of YSGG is similar to that of LuSGG:Cr and is not shown in the Fig. 4. The R-line emission of YSGG:Cr is slightly red shifted, if compared to LuSGG:Cr and appears at around 690 nm. In GSGG:Cr, the $^4T_2$ broad band and ^2E line emission coexist at 3 K. The broad band at low temperature is still dominant in comparison to the weak R-line emission located at 694.5 nm. It points to a small energy separation between ^2E and $^4T_2$ levels and both broad band and Cr^{3+} line emission can be observed at low temperature [36].

The appearance of the R-line emission in LuSGG:Cr, YSGG:Cr, and GSGG:Cr at liquid helium temperature allow us to classify these garnets to materials with intermediate crystal field strength ($2.4 < Dq/B < 2.6$), where the ^2E level lies below the $^4T_2$ level. Since the position of the $^4T_2$ zero-phonon lines (ZPL) in these phosphors cannot be observed even at 3 K, the positions of the ZPLs were estimated from the symmetry of the absorption and emission band shapes. Based on these estimates, the energy difference between the ^2E and $^4T_2$ zero-phonon lines in these garnets was determined to be 686 cm^{-1}, 466 cm^{-1}, 147 cm^{-1}, respectively.

In the low temperature emission spectrum of LaSGG:Cr, only the NIR broad band emission resulting from the $^4T_2 \rightarrow {}^4A_2$ transition is observed. The absence of the ^2E emission at 3 K in LaSGG:Cr indicates that the $^4T_2$ zero-vibrational level lies below the ^2E level (weak crystal field, $Dq/B \sim 2.3$). The energy of the ^2E level (14492 cm^{-1}) was determined from Fano type interactions between intraconfigurational ^2E and $^4T_2$ levels apparent as dips in the excitation spectrum recorded at 3 K. Based on this estimate, the energy gap between $^4T_2$ and ^2E zero-vibrational transition was evaluated and amounts to $-$ 874 cm^{-1}.

The Cr^{3+} R-line emission in LuSGG, YSGG, and GSGG garnets (Fig. 4 and Fig. 5) shifts to longer wavelengths (lower energy) with increase of the lattice constants (decreasing crystal field). From the Tanabe Sugano diagram for the $3d^3$ electron configuration in the octahedral crystal field it can be noticed that the energy of the ^2E level has a small dependence on the crystal field strength, and its energy is nearly equal to the energy of the ^2G term of a free ion. The energy of the doublet level can be expressed by the following equation $E(^2E) = 3.05C + 7.9B - 1.8B^2/Dq$ [37]. Assuming a negligible influence of the Dq parameter on the ^2E level energy, only the B and C Racah parameters determine the energy of the $^2E \rightarrow {}^4A_2$ transition. Indeed, the nephelauxetic effect that involves delocalization of the outer d electrons over the p- and s-orbitals of the ligands causes a decrease of the repulsion forces within the d shell and results in a decrease of the B and C parameters. The reduction of Racah parameters depends not only on the nature of ligands, but also on the interionic distances and bonding angles. Therefore, a different degree of B and C reduction in various Cr-doped materials is observed and the nephelauxetic effect is the main factor impacting the variation of the energies of the $^2E \rightarrow {}^4A_2$ transition in different host lattices [38]. For instance, the emission R-lines in $LaSc_3(BO_3)_4$ (B = 675 cm^{-1}, C = 3448 cm^{-1}) [39], $Al_2O_3:Cr^{3+}$ (B = 640 cm^{-1}, C = 3300 cm^{-1}) [38], $ZnWO_4:Cr^{3+}$ (B = 669 cm^{-1}, C = 3060 cm^{-1}) [40], $LaGaO_3:Cr^{3+}$ (B = 589 cm^{-1}, C = 3077 cm^{-1}) [38], $LaAlO_3$ (B = 663 cm^{-1}, C = 2908 cm^{-1}) [41], $CaYAlO_4:Cr^{3+}$ (B = 705 cm^{-1}, C = 2750 cm^{-1}) [42] are located at 684 nm, 694 nm, 714 nm, 729 nm, 734 nm, and 742 nm respectively. This

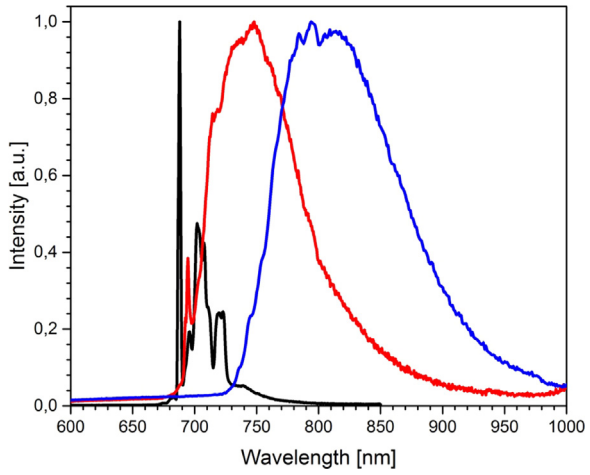

Fig. 4. Emission spectra of LuSGG:1%Cr^{3+} (black line), GSGG:1%Cr^{3+} (red line), and LaSGG:1%Cr^{3+} (blue line) measured at 3 K upon excitation at 440 nm, 460 nm, and 480 nm, respectively.

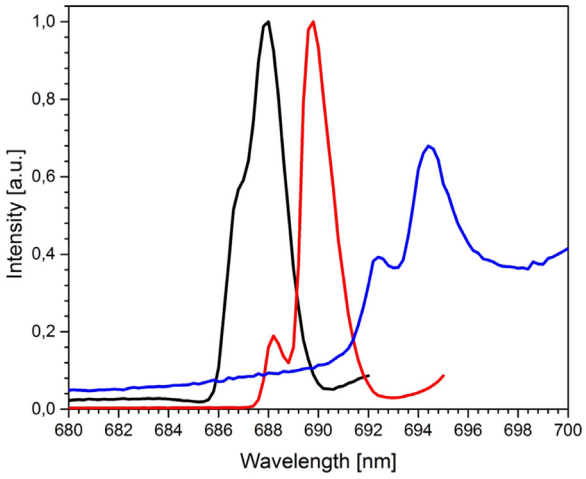

Fig. 5. High resolution ^2E photoluminescence spectrum of Cr^{3+} ions in LuSGG (black line), YSGG (red line), and GSGG (blue line) measured at 3 K upon excitation at 440 nm, 450 nm, and 460 nm, respectively.

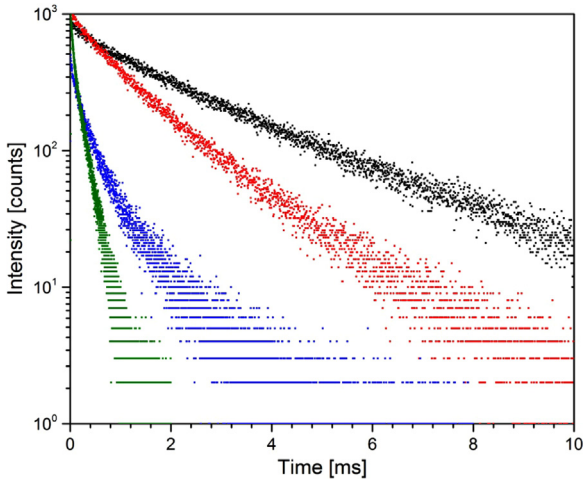

Fig. 6. Decay time curves (a) of Cr^{3+} emission in LuSGG (black dots), YSGG (red dots), GSGG (blue dots), LaSGG (green dots) measured at 3 K. Monitored excitation and emission wavelengths are collected in Table 5.

points out, that the position of the ZPL transition $^2E \rightarrow {}^4A_2$ can be tuned over 60 nm. The Racah parameter *B* in the various Cr^{3+}-doped materials mentioned above does not have a clear relation to the ^2E spectral position, whereas the Racah parameter *C* gradually decreases as the red shift of the R-lines increases. The experimental data for LuSGG, YSGG and GSGG show that the change of the *C* parameters along the series is greater than the change of the *B* parameters (Table 3). Therefore, we attribute the red shift of the ^2E emission peaks to the decrease of the *C* Racah parameter.

The high resolution emission spectra of Cr^{3+} ions in LuSGG, YSGG, and GSGG measured between 680 and 700 nm at 3 K are displayed in Fig. 5 and reveal two ^2E zero-phonon lines. In LuSGG:Cr an overlap of two peaks can be observed indicating a small energy difference between the peaks. In YSGG:Cr and GSGG:Cr two distinct lines separated by 42 cm^{-1} are seen. The R-lines in the chromium doped XSGG garnets are unusual broad. The FWHM for the most intense peaks are around 30 cm^{-1}. The presence of two broadened R-lines in the emission spectra at liquid helium temperature may result from inhomogeneous broadening of the R-line due to a local crystal lattice disorder associated with a partial substitution of Sc^{3+} ions by the smaller Ga^{3+} ions on the octahedral sites. The same phenomenon was observed by B. Henderson et al. in GSGG:Cr where the presence of two sets of R-lines was explained by emission from 'normal' Cr^{3+} and Cr^{3+} ions with a Ga-neighbor on a Sc-site [43]. In addition to giving rise to two distinct Cr^{3+} emission lines, the Ga-Sc substitution was observed to give rise to inhomogeneous broadening of both R-lines.

Since the fluorescence decay time of the Cr^{3+} emission strongly depends on the temperature, we measured decay time curves at liquid helium temperature. Fig. 6 displays low temperature decay curves of ^2E emission of Cr^{3+} ions in XSGG (X = Lu, Y, Gd) and a decay curve of $^4T_2$ emission of Cr^{3+} in LaSGG. The emission was monitored at specific wavelengths upon pulsed blue excitation (Table 5). The decay curves are close to single exponential. The observation of a slightly non-exponential decay can be assigned to the aforementioned disorder.

Table 5
Decay time of the Cr^{3+} emission in XSGG (X = Lu, Y, Gd, La) garnets determined from the decay curves measured at 3 K and at room temperature. λ_{exc} and λ_{em} are excitation and emission wavelengths and ΔE is the energy separation between ^2E and $^4T_2$ zero-vibrational lines.

	λ_{exc}	λ_{em}	τ_{3K} [μs]	τ_{300K} [μs]	ΔE
LuSGG	450	688	2200	314	686 cm^{-1}
YSGG	460	690	1200	125	466 cm^{-1}
GSGG	470	694	425	102	147 cm^{-1}
LaSGG	480	780	178	104	− 874 cm^{-1}

The lifetimes of the R-line at 3 K for Cr^{3+} doped LuSGG and YSGG are in the *ms* range, typical of the spin- and parity-forbidden $^2E \rightarrow {}^4A_2$ transition (Table 5). The lifetime for the ^2E emission in GSGG:Cr is lowered to the *μs* range (425 μs) and is close to that for the $^4T_2$ emission in LaSGG:Cr (178 μs). The decay time of the ^2E emission exhibits a strong variation with the ΔE energy separation between the two low lying ^2E and $^4T_2$ levels. The decrease of the ΔE from 686 cm^{-1} for LuSGG:Cr to 147 cm^{-1} for GSGG:Cr corresponds to the lowering of the decay rate from 2.2 ms to 425 μs. The smaller energy separation between the ^2E and $^4T_2$ states induces greater mixing of these states and a shorter decay time of ^2E emission is observed. In LaSGG:Cr Cr^{3+} ions occupy a weak crystal field site and the lowest excited state is $^4T_2$ state (ΔE < 0). The spin-allowed and parity forbidden $^4T_2 \rightarrow {}^4A_2$ transition has a shorter decay time as the decay time of LaSGG:Cr is mostly determined by radiative and non-radiative processes of the spin-allowed and parity forbidden $^4T_2 \rightarrow {}^4A_2$ transition [44].

It is also interesting to investigate the fine structure of the broad emission bands at 3 K and to compare the values of the phonon-coupling parameters for the four different garnet structures. At low temperature the broad band emission spectra of GSGG:Cr and LaSGG:Cr are narrower than at RT. The FWHM values for GSGG:Cr and LaSGG:Cr are 83 nm (~ 1450 cm^{-1}) and 115 nm (~ 1750 cm^{-1}), respectively. This confirms the stronger electron-phonon coupling for the $^4T_2 \rightarrow {}^4A_2$ transition in LaSGG. In the emission spectrum of LaSGG:Cr (Fig. 4) four peaks are visible with maximum at around 735 nm (13,605 cm^{-1}), 745 nm (13,423 cm^{-1}), 755 nm (13,245 cm^{-1}), and 765 nm (13,072 cm^{-1}). The peak at 735 nm is assigned to the $^4T_2 \rightarrow {}^4A_2$ zero-phonon line transition, whereas the peaks at longer wavelengths can be attributed to the phonon satellites of the ZPL. The energy difference between ZPL and its phonon satellites was determined to be ~ 180 cm^{-1} and this is one of the vibrational modes that couple with the $^4T_2 \rightarrow {}^4A_2$ transition.

From the photoluminescence spectra recorded at 3 K, the values for Stokes shift and Huang-Rhys parameter *S* can be determined more precisely because of the negligible thermal broadening at low temperature. The Stokes shift was determined from the energy difference between the excitation and emission maxima ($\Delta E_{ss} = E(^4A_2 \rightarrow {}^4T_2) - E(^4T_2 \rightarrow {}^4A_2)$) to be ~ 2400 cm^{-1}, whereas the Huang-Rhys parameters was estimated from the relative intensity of the zero-phonon line and amounts to ~ 6 [45]. This value of 6 is consistent with the observed Stokes shift and a vibrational energy of ~ 180 cm^{-1} giving a Stokes shift of $(2S+1)\ \hbar\omega$ of 2340 cm^{-1}. The Huang-Rhys parameters *S* for the $^4T_2 \rightarrow {}^4A_2$ transition for Cr^{3+} in the other XSGG (X = Lu, Y, Gd) garnets cannot easily be determined as there is no zero-phonon line observed in the $^4T_2 \rightarrow {}^4A_2$ emission spectra due to the ^2E emission. Based on the narrower spectral widths of the $^4T_2 \rightarrow {}^4A_2$ transition the Huang-Rhys parameter *S* can be estimated to be between 4 and 5, but the uncertainty is high.

3.5. Temperature dependent Cr^{3+} luminescence of $X_3Sc_2Ga_3O_{12}$:Cr between 77 and 800 K

To investigate the thermal quenching behavior of the emission temperature dependent emission spectra and temperature dependent lifetime measurements were performed. The temperature dependence of the emission intensity was recorded under identical alignment conditions between 77 and 800 K for Cr^{3+}-doped LaSGG, YSGG, and GSGG, and between 77 and 500 K for LaSGG.

Fig. 7 displays the normalized integrated emission intensity of the Cr^{3+} emission in XSGG (X = Lu, Y, Gd, La) as a function of temperature. In the case of LuSGG:Cr, YSGG:Cr, and GSGG:Cr the thermal quenching does not start until high temperatures, viz. ~ 450 K. In the low temperature region, the emission intensity slightly increases. It can be associated with an increase in the radiative decay rate due to thermal population of the $^4T_2$ level. An increase in radiative transition

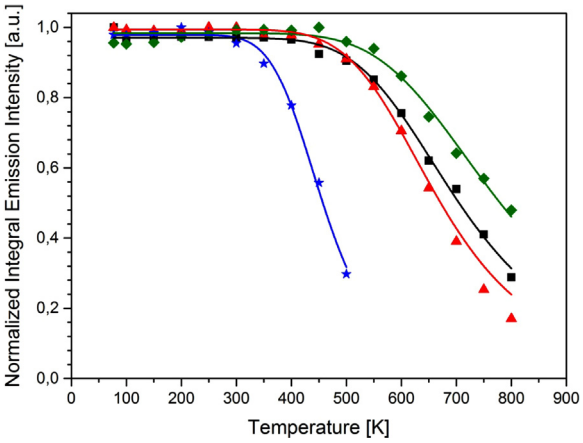

Fig. 7. Normalized integral emission intensity of Cr^{3+} doped LuSGG (black squares), YSGG (red triangles), GSGG (green rhombs), and LaSGG (blue stars) as a function of temperature between 77 and 800 K. The drawn lines correspond to the Fermi-Dirac fit of the experimental data.

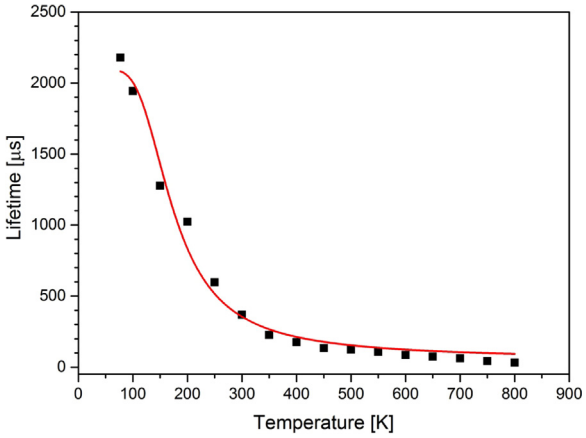

Fig. 8. Temperature dependence of the decay time of the R-line emission (688 nm) in LuSGG:Cr determined from the single exponential fits of the decay curves. The drawn line is a fit to a Boltzmann equation.

probability combined with a temperature independent non-radiative decay rate from this state can explain the intensity increase and has also been observed before e.g., in $YAl_3(BO_4)_3$:Cr [26]. Alternatively, an increase in absorption strength due to an increase in phonon-assisted absorption for the parity forbidden $^4A_2 \rightarrow {}^4T_1$ absorption transition can also explain the small increase in intensity. In order to determine the quenching temperature ($T_{1/2}$ is the temperature where the emission intensity reaches 50% of its maximum) a Fermi-Dirac fit $I(T) = I_0/[1 + B{\cdot}\exp(-\Delta E_{act.}/kT)]$ was used, where I(T) is the PL intensity at a certain temperature, I_0 is the PL intensity at 0 K, B is the frequency factor for thermal quenching, ΔE_{act} is the activation energy for thermal quenching, k is the Boltzmann constant, and T is the temperature. The quenching temperatures were calculated based on the $T_{1/2} = -\Delta E_{act.}/k{\cdot}\ln(1/B)$ formula. The obtained $T_{1/2}$ values for the Cr^{3+} emission in LuSGG, YSGG, and GSGG are 714 K, 660 K, and 780 K, respectively. The high $T_{1/2}$ values confirm the superior thermal stability of the chromium luminescence in these garnet type hosts and brands these phosphors as suitable for highly efficient diode pumped broad band NIR sources between 650 and 850 nm.

In LaSGG Cr^{3+} ions occupy a weak crystal field site and the $^4T_2$ level lies below the ^2E level. Due to a lower energy position of the excited state a lower quenching temperature for the chromium emission is expected [46]. In addition, the larger spectral width (in cm^{-1}) and corresponding higher Huang-Rhys parameter reveal a stronger electron-phonon coupling for Cr^{3+} in LaSGG compared to the other garnets. This will also contribute to a lowering of the luminescence quenching temperature. Indeed, the thermal quenching behavior in LaSGG:Cr diverges from that observed in XSGG:Cr (X = Lu, Y, Gd). The thermal quenching of the $^4T_2$ luminescence of Cr^{3+} starts at lower temperature, viz. 300 K. The quenching temperature determined from the Fermi-Dirac fit is 450 K. The value of the $T_{1/2}$ for the Cr^{3+} emission in LaSGG is ca. 200 K lower than the quenching temperatures in other three garnets. However, to the best of our knowledge, there are no reports on such high quenching temperature obtained for the broad band NIR emission of chromium extending to 1000 nm. For example, the thermal quenching of the broad band NIR emission of Cr^{3+} in $CaSc_2O_4$ sets in already at 77 K and at ~ 240 K the emission intensity decreases to 50% of the 77 K value [20].

To further investigate the thermal quenching behavior, luminescence lifetimes of the Cr^{3+} emission were recorded as a function of temperature between 77 and 800 K. Fig. 8 reveals the temperature dependence of the decay time of the $^2E/^4T_2$ emission in LuSGG:Cr. The decay times were determined from the single exponential fitting of the decay curves measured for the 688 nm emission upon pulsed excitation at 440 nm. The temperature dependence of the Cr^{3+} luminescent lifetime can be described by the Boltzmann equation $1/\tau_2(T) = 1/\tau_2(0) + 3/\tau_4{\cdot}\exp(-\Delta E/kT)$, where ΔE is the zero-phonon line $^4T_2$–^2E energy separation, k is the Boltzmann constant, τ_4 and $\tau_2(0)$ are the radiative lifetimes of $^4T_2$ and ^2E states, respectively [47]. The best fit of the Boltzmann equation to the data is displayed as a solid line in Fig. 8. As can be observed, the decay time strongly decreases between 77 and 300 K. The lifetime of the Cr^{3+} emission decreased from ~ 2.1 ms to 360 µs, respectively. The shortening of the lifetime cannot be due to a non-radiative quenching of the Cr^{3+} photoluminescence, since the emission intensity remains constant over the same temperature range. The strong reduction of the decay time is related to much higher decay rate of the spin-allowed $^4T_2 \rightarrow {}^4A_2$ transition, which appears due to the increased equilibrium population in the $^4T_2$ state at higher temperatures [48].

In GSGG:Cr and LaSGG:Cr, the variation of the Cr^{3+} luminescence lifetime with temperature is not as large because of the smaller energy separation between ^2E and $^4T_2$ levels which results for GSGG already at 3 K for a dominant emission from the $^4T_2$ state and a shorter life time.

From the Boltzmann fit of the temperature dependent decay time the zero-phonon line ^2E-$^4T_2$ energy separation was determined to be ~ 0.061 eV. As obtained ΔE value is lower than the ZPL energy separation estimated from the symmetry of the luminescence spectra of LuSGG:Cr (ΔE ~ 0.085 eV). It can indicate on a quite high uncertainty of the later method in the estimation of the position of the $^4T_2$ zero-phonon line.

The quenching temperature of the $^4T_2$ emission of Cr^{3+} in the garnets is higher than the previously reported quenching temperatures for the broad band $^4T_2$ emission of Cr^{3+}. To understand the high quenching temperatures for the Cr^{3+} emission the Stokes shift which is a measure of the electron-phonon coupling strength is considered and related to the activation energy for the thermal quenching as determined from the Fermi-Dirac fit of the experimental data (Fig. 7). In general, a smaller Stokes shift results in a higher quenching temperature. The Stokes shift in the investigated Cr-garnets was determined from the low temperature luminescence spectra and is ca. 2400 cm^{-1}. It turns out that the Stokes shift of the Cr^{3+} emission in the Ga-garnets is smaller than the Stokes shift in $YAl_3(BO_4)_3$:Cr (ΔE_{ss} = 2862 cm^{-1}, $T_{1/2}$ = 620 K) [26] or in $CaSc_2O_4$:Cr (ΔE_{ss} = 3042 cm^{-1}, $T_{1/2}$ < 240 K) [20] which is consistent with the higher luminescence quenching temperatures of ~ 700 K.

The quenching temperature for the $^4T_2$ emission in LaSGG:Cr is 450 K. The lower $T_{1/2}$ value in comparison to the other Cr-garnets is due to the stronger electron-phonon coupling strength in LaSGG:Cr which is evident from the broader spectral width of the $^4T_2$–$^4A_2$ emission band at

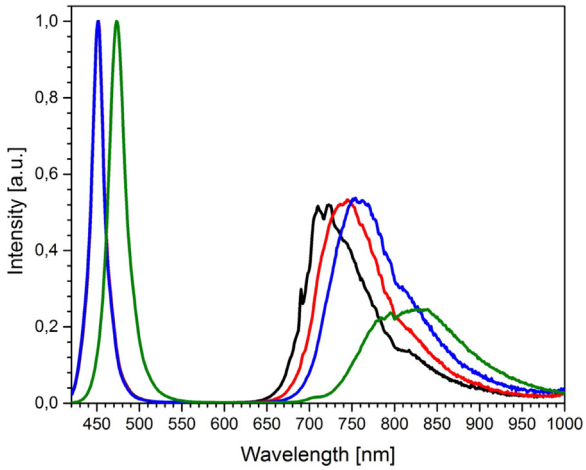

Fig. 9. Normalized emission spectra of LuSGG:Cr (black line), YSGG:Cr (red line), GSGG:Cr (blue line), and LaSGG:Cr (green line) ceramic pellets measured upon 451 nm (for LuSGG, YSGG, and GSGG) and 474 nm (for LaSGG) LED excitation (0.13 A, 2.8 V), respectively. The emission spectra were normalized for the maximum emission intensity of the blue LEDs.

RT (2160 cm^{-1} in LaSGG vs. ~ 1500 cm^{-1} in the other garnets). This is in line with the difference in Huang-Rhys coupling parameter *S*, which is estimated be close to 6 for the $^4T_2 \rightarrow {}^4A_2$ emission in LaSGG and between 4 and 5 for the other garnets (vide supra). Due to the stronger electron-phonon coupling activation energy for thermal quenching is lower for the $^4T_2$ emission of Cr^{3+} in LaSGG ($\Delta E_{act.}$ = 0.36 eV for LaSGG:Cr, $\Delta E_{act.}$ = 0.42 eV for GSGG:Cr). An additional factor contributing to the lower activation energy for thermal quenching of the emission in LaSGG:Cr is the lower energy position of the Cr^{3+} emission band. From the work of Blasse it is well-known that for the same electron-phonon coupling, a lower energy excited state gives rise to lower luminescence quenching temperatures.

The present results on broad band NIR emission show very favorable thermal quenching behavior for broad band NIR emission. For the 650–850 nm emission $X_3Sc_2Ga_3O_{12}$:Cr (X = Y, Gd, Lu) the quenching temperatures exceed 600 K while for the 700–1000 nm emission of Cr^{3+} in $La_3Sc_2Ga_3O_{12}$ emission from the $^4T_2$ level does not quench up to 300 K which is a very high quenching temperature for such red shifted broad band emission (FWHM = 145 nm at RT) with maximum at around 818 nm. Further tuning of the spectral emission range and optimization of the quenching temperature can be achieved in mixed $(La,X)_3Sc_2Ga_3O_{12}:Cr^{3+}$ (X = Y, Gd, Lu) garnets, again demonstrating the unique tunability of optical properties in garnets through variations in the cation sublattices [49]. It is evident that the efficient broad band NIR $^4T_2$ emission from Cr^{3+} is scandium gallium garnets is promising for the development of efficient broad band diode-pumped NIR light sources. In the next section the feasibility of this type of NIR light source is demonstrated.

3.6. NIR LEDs with $X_3Sc_2Ga_3O_{12}:Cr^{3+}$ (X = Lu, Y, Gd, La) pellets

To demonstrate the capability of Cr^{3+} garnets for application in NIR pcLEDs, ceramic pellets for emission measurements were prepared. The diameter and thickness of the pellets were 13 mm and ca. 1 mm, respectively. The pellets of LuSGG:Cr, YSGG:Cr, and GSGG:Cr were opaque, whereas the pellet of LaSGG was translucent. As excitation sources, 451 nm (for LuSGG, YSGG, GSGG) and 474 nm (for LaSGG) high power (In,Ga)N LEDs were used which excite the Cr^{3+} ions at a wavelength close to the maximum of the $^4A_2 \rightarrow {}^4T_1$ (^4F) absorption band. The Cr^{3+} concentration is 1%.

Fig. 9 displays emission spectra obtained upon irradiation of the pellets by the blue LEDs at a drive current of 0.13 A. The emission spectra consist of two spectral components, one in the blue (LED chip) and one in the NIR region (Cr-phosphor). The integral emission intensities of the NIR emission of Cr^{3+} in LuSGG, YSGG, GSGG are ~ 2.6 times larger than the blue light integral emission intensity. In LaSGG:Cr, the NIR/blue ratio is two times smaller ~ 1.3 and may be due to a higher transmission of blue light passing the translucent pellet (weaker light scattering than in opaque pellets). Alternatively, the lower NIR/blue ratio can be due to the lower quantum efficiency (QE) of starting material used for the pellet making. The QE values for XSGG:Cr (X = Lu, Y, Gd) are ~ 60%, while the QE for LaSGG:Cr is 35%.

We have also determined the conversion efficiency of ceramic pellets. It turned out, that the blue to NIR conversion efficiency is lower than 5%. Such rather low phosphor conversion efficiency may be caused by the loss of blue light in the constructed sample holder due to a backscattering and reflection of incident light by pellets back to the LED chip and housing. Thus, for a more precise estimation of blue to NIR conversion efficiency by Cr-doped garnets, a true NIR pcLED device should be constructed in which the backscattering and backreflection will be minimized e.g., by the optimization of phosphor particle size.

4. Conclusions

The photoluminescence of Cr^{3+} in XSGG (X = Lu, Y, Gd, La) was investigated between 3 K and 800 K. In $Lu_3Sc_2Ga_3O_{12}$, $Y_3Sc_2Ga_3O_{12}$, and $Gd_3Sc_2Ga_3O_{12}$ the local coordination of Cr^{3+} gives rise to an intermediate crystal field where the $^4T_2$ level is just above the ^2E level. In $La_3Sc_2Ga_3O_{12}$ a weak crystal field is observed. At room temperature all Cr^{3+}-doped scandium gallium garnets display efficient broad band NIR emission due to the $^4T_2 \rightarrow {}^4A_2$ transition. The luminescence properties (intensities and lifetimes) of the Cr^{3+} emission in garnets are strongly affected by the energy separation between the ^2E and $^4T_2$ levels. The increase of the lattice parameters in Cr-garnets causes a red shift of the emission due to a lowering the energy of the $^4T_2$ level in a weaker crystal field. The emission spectrum of LaSGG:Cr (Dq = 1458 cm^{-1}) is red shifted by about 100 nm in comparison to the spectrum of LuSGG (Dq = 1626 cm^{-1}). The quenching temperature of the broad band $^4T_2$ emission in XSGG (X = Lu, Y, Gd) is high viz. $T_{1/2}$ ~ 700 K. The high thermal stability of Cr^{3+} emission is consistent with a small Stokes shift (~ 2400 cm^{-1}) and a weak electron-phonon coupling strength, reflected by a small Huang-Rhys parameter (S = 4–5). The quenching temperature for $^4T_2$ emission in LaSGG:Cr ($T_{1/2}$ = 450 K) is lower due to the stronger electron-phonon strength (S = 6). The efficient broad band NIR emission with high thermal quenching temperatures make Cr^{3+}-doped XSGG (X = Lu, Y, Gd, La) promising materials for application in phosphor converted (In,Ga)N LEDs for high power broad band NIR sources in the 650–1000 nm range.

Acknowledgements

The authors are grateful to Merz Pharmaceuticals GmbH for generous financial support.

References

[1] S. Nakamura, T. Mukai, M. Senoh, Appl. Phys. Lett. 64 (1994) 1687.
[2] J. Cho, J.H. Park, J.K. Kim, E.F. Schubert, Laser Photonics Rev. 11 (2017) 1600147.
[3] S. Ye, F. Xiao, Y.X. Pan, Y.Y. Ma, Q.Y. Zhang, Mater. Sci. Eng. R 71 (2010) 1.
[4] Y. Tian, J. Solid State Light. 1 (2014) 11.
[5] Y. Lee, C. Lee, C. Chen, J. IEEE Quantum Electron 46 (2010) 1450.
[6] G. Blasse, B.C. Grabmaier, Luminescent Materials, Springer-Verlag, Berlin, 1994.
[7] A. Lakshmanan, Luminescence and Display Phosphors: Phenomena and Applications, Nova Science Publishers, New York, 2008.
[8] T.-Y. Seong, J. Han, H. Amano, H. Morkoç, III-Nitride Based Light Emitting Diodes and Application, Springer, New York, 2013.
[9] A.A. Setlur, A.M. Srivastava, H.A. Comanzo, G. Chandran, H. Aiyer, M.V. Shankar, S.E. Weaver, Proc. SPIE 5187 (2004) 142.
[10] X. Piao, K. Machida, T. Horikawa, H. Hanzawa, Y. Shimomura, N. Kijima, Chem. Mater. 19 (2007) 4592.
[11] V. Bachmann, T. Jüstel, A. Meijerink, C. Ronda, P.J. Schmidt, J. Lumin. 121 (2006) 441.

[12] L. Liu, R.-J. Xie, N. Hirosaki, T. Takeda, J. Li, X. Sun, J. Am. Ceram. Soc. 92 (2009) 2668.
[13] B. Malysa, T. Jüstel, D. Uhlich, I. Becker, H. Bettentrup, Infrared LED, DE102014107321 A1, 2015.
[14] J. Malinen, M. Känsäkoski, R. Rikola, C.G. Eddison, Sens. Actuators B 51 (1998) 220.
[15] B.A. Russell, N. Kellett, L.R. Reilly, J. Cosmet. Laser Ther. 7 (2005) 196.
[16] A. Unterhuber, B. Povazay, K. Bizheva, B. Hermann, H. Sattmann, A. Stingl, T. Le, M. Seefeld, R. Menzel, M. Preusser, H. Budka, C. Schubert, H. Reitsamer, P.K. Ahnelt, J.E. Morgan, A. Cowey, W. Drexler, Phys. Med. Biol. 49 (2004) 1235.
[17] H. Liu, D.A. Boas, Y. Zhang, A.G. Yodh, B. Chance, Phys. Med. Biol. 40 (1995) 1983.
[18] T.W.L. Scheeren, P. Schober, L.A. Schwarte, J. Clin. Monit. Comput. 26 (2012) 279.
[19] C.B. Han, C. He, X.J. Li, Adv. Mater. 23 (2011) 4811.
[20] B. Malysa, A. Meijerink, W. Wu, T. Jüstel, J. Lumin. 190 (2017) 234.
[21] B. Struve, G. Huber, Appl. Phys. B 36 (1985) 195.
[22] Z. Kristallog, 125(1), 1967.
[23] R.D. Shannon, Acta Cryst. A32 (1976) 751.
[24] R.G. Burns, Mineralogical Applications of Crystal Field Theory, second ed., Cambridge University Press, Cambridge, 1993.
[25] P. Villars, K. Cenzual, Pearson's Crystal Data: Crystal Structure Database for Inorganic Compounds, Release 2017/18, ASM International*, Materials Park, Ohio, USA.
[26] B. Malysa, A. Meijerink, T. Jüstel, J. Lumin. 171 (2016) 246–253.
[27] S. Sakirzanovas, A. Katelnikovas, H. Beltrup, A. Kareiva, T. Jüstel, J. Lumin. 131 (2011) 1525.
[28] M.H. Krisch, C.C. Kao, F. Sette, W.A. Caliebe, K. Hämäläinen, J.B. Hastings, Phys. Rev. Lett. 7 (1995) 4931.
[29] K.O. Ruotsalainen, A.-P. Honkanen, S.P. Collins, G. Monaco, M. Moretti Sala, M. Krisch, K. Hämäläinen, M. Hakala, S. Huotari, Sci. Rep. 6 (2016) 22648.
[30] J. He, H. Liang, D. Hou, S. Sun, Y. Huang, Z. Gao, Y. Tao, Mater. Chem. Phys. 132 (2012) 756.
[31] Y. Kalisky, The Physics and Engineering of Solid State Lasers, SPIE – The International Society for Optical Engineering, Washington, 2006.
[32] K.M. Kinsman, J. McKittrick, J. Am. Ceram. Soc. 77 (1994) 2866.
[33] K.P. O'Donnell, A. Marshall, M. Yamaga, B. Henderson, J. Lumin. 42 (1989) 365.
[34] C.P. Poole, J. Phys. Chem. Solids 25 (1964) 1169.
[35] A. Trueba, P. Garcia-Fernandez, J.M. Garcia-Lastra, J.A. Aramburu, M.T. Barriuso, J. Phys. Chem. A 115 (2011) 1423.
[36] M. Yamaga, B. Henderson, K.P. O'Donnell, G. Yue, Appl. Phys. B 51 (1990) 132.
[37] J. García Solé, L.E. Bausá, D. Jaque, An Introduction to the Optical Spectroscopy of Inorganic Solids, John Wiley & Sons Ltd, England, 2005.
[38] M.G. Brik, S.J. Camardello, A.M. Srivastava, N.M. Avram, A. Suchocki, ECS J. Solid State Sci. Technol. 5 (2016) R3067.
[39] X. Long, Z. Lin, Z. Hu, G. Wang, T.P.J. Han, J. Alloy Compd. 347 (2002) 52.
[40] E. Cavalli, A. Belletti, M.G. Brik, J. Phys. Chem. Solids 69 (2008) 29.
[41] Y. Katayama, J. Ceram. Soc. Jpn. 125 (2017) 793.
[42] M. Yamaga, P.I. Macfarlane, K. Holliday, B. Henderson, N. Kodama, Y. Inoue, J. Phys.: Condens. Matter 8 (1996) 3487.
[43] B. Henderson, K.P. O'Donnell, M. Yamaga, B. Cockayne, M.J.P. Payne, AIP Conf. Proc. 172 (1988) 425.
[44] Z. Zhang, K.T.V. Grattan, A.W. Palmer, Phys. Rev. B 48 (1993) 7772.
[45] B. Henderson, G.F. Imbusch, Optical spectroscopy of solids, Oxford University Press, Oxford, 1989.
[46] G.F. Imbusch, T.J. Glynn, G.P. Morgan, J. Lumin. 45 (1990) 63.
[47] M. Grinberg, Phys. Status Solidi A 130 (1992) K189.
[48] S.M. Healy, C.J. Donnelly, T.J. Glynn, G.F. Imbusch, G.P. Morgan, J. Lumin. 46 (1990) 1.
[49] J. Xu, J. Ueda, S. Tanabe, J. Am. Ceram. Soc. 100 (2017) 4033.